



# A low-temperature solid-to-solid reaction for lithium-ion battery recycling and the utilization of defect-enriched $\text{Co}_3\text{O}_4$ from spent $\text{LiCoO}_2$ batteries for efficient oxygen evolution reaction

Zhizhou Wang<sup>a,b,1</sup>, Zebiao Li<sup>c,1</sup>, Jing Zhong<sup>d,1</sup>, Binbin Zhou<sup>e</sup>, Jie Liu<sup>a,\*</sup>, Jie Pan<sup>f</sup>, Feng Cao<sup>a</sup>, Jianbin Lin<sup>g</sup>, Zheming Zhang<sup>b,\*</sup>, Haidong Bian<sup>b,\*</sup>

<sup>a</sup> School of Chemistry and Life Sciences, Suzhou University of Science and Technology, Suzhou, Jiangsu 215009, China

<sup>b</sup> Shenzhen Automotive Research Institute, Beijing Institute of Technology, Shenzhen, Guangdong 518118, China

<sup>c</sup> PetroChina Shenzhen New Energy Research Institute Co. LTD, Shenzhen 518052, China

<sup>d</sup> Department of Materials Science and Engineering, City University of Hong Kong, Hong Kong, SAR China

<sup>e</sup> Shenzhen Institute of Advanced Electronic Materials, Shenzhen Institute of Advanced Technology, Chinese Academy of Sciences, Shenzhen 518055, China

<sup>f</sup> School of Flexible Electronics (Future Technologies), Institute of Advanced Materials, Jiangsu National Synergetic Innovation Center for Advanced Materials, Nanjing Tech University, Nanjing 211816, China

<sup>g</sup> CityU-Shenzhen Futian Research Institute, Shenzhen 518045, China

## ARTICLE INFO

### Keywords:

Li battery recycling  
 $\text{LiCoO}_2$   
 $\text{Co}_3\text{O}_4$   
Oxygen and cobalt vacancy  
Oxygen evolution reaction

## ABSTRACT

An efficient, eco-friendly and cost-effective strategy for the recovery of precious metals from spent lithium-ion batteries (LIBs) is of great significance for the sustainable natural resource utilization and environmental protection. Herein, a low-temperature solid-to-solid reaction combined water leaching technology is proposed for the preferential extraction of Li from spent  $\text{LiCoO}_2$  batteries. In the solid-to-solid reaction, crystal water released from the oxalic acid dihydrate acts as a lubricant and initiates the reduction reaction to convert the spent  $\text{LiCoO}_2$  into water-soluble Li salts ( $\text{LiHC}_2\text{O}_4$  or  $\text{Li}_2\text{C}_2\text{O}_4$ ) and water-insoluble  $\text{CoC}_2\text{O}_4$ . After water leaching, the collected Li-rich solution and the Co-rich residue are separately transformed into  $\text{Li}_2\text{CO}_3$  and  $\text{Co}_3\text{O}_4$ . Additionally, a defect-enriched  $\text{Co}_3\text{O}_4$  is prepared by water quenching process, exhibiting excellent performances towards oxygen evolution reaction. This work not only achieves a facile, low-cost and energy-saving strategy for recycling spent LIBs, but also proposes a vacancy-defected engineering route for electrocatalyst design in energy-related applications.

## 1. Introduction

Electric vehicles (EVs) are becoming increasingly popular around the world, which has skyrocketed demand for Li-ion batteries (LIBs). It has been estimated that the global demand for LIBs is expected to increase from about 700 GWh (over 3.6 million tons) in 2022 to around 4.7 TWh (over 24.6 million tons) by 2030.[1] In the coming years, scrapped LIBs will significantly increase since their lifetime ranges from 3 to 8 years. [2] The proper disposal of spent LIBs not only alleviates the ecological impact but also prevents the loss of precious metals, such as Li, Co, Ni, and Cu.[3] Pyrometallurgy, hydrometallurgy, or a combination of the two are the most prevalent strategies for recovering metals from spent LIBs.[4] Other techniques, like electrochemical exfoliation,[5,6] have

been created but are limited by their production scale constraints. A typical pyrometallurgical process involves melting the whole spent LIB at a high temperature over 1000 °C to form a metal alloy.[7] Nevertheless, this technology is subject to the drawbacks of having a high energy demand, hazardous gas emissions, and an unacceptable loss of lithium. In recent years, the hydrometallurgical process has been widely used for recycling LIBs as a result of its high metal recovery efficiencies and purity.[8] Despite this, a considerable amount of acidic wastewater and by-products (hazardous gases, leaching residues, etc.) are generated, which require additional tedious post-treatment. Further, lithium salt is usually precipitated in the last step of conventional hydrometallurgical processes, which inevitably results in a loss of Li in the aqueous solution.

\* Corresponding authors.

E-mail addresses: [jliu@mail.usts.edu.cn](mailto:jliu@mail.usts.edu.cn) (J. Liu), [zhangzheming@szari.ac.cn](mailto:zhangzheming@szari.ac.cn) (Z. Zhang), [bhd.555@hotmail.com](mailto:bhd.555@hotmail.com) (H. Bian).

<sup>1</sup> These authors contributed equally.

To improve Li recovery rate, a thermal reduction combined water leaching (reducing-roasting-leaching) method has been recently developed for preferentially leaching lithium from spent LIBs. In a typical reaction, a reduction roasting process is applied first to treat spent cathode powders, in which Li is transformed into water-soluble salt ( $\text{Li}_2\text{CO}_3$  or  $\text{Li}_2\text{O}$ ) and Co (Ni and Mn) is reduced to water-insoluble metal or metal oxides ( $\text{CoO}$ ,  $\text{Co}_3\text{O}_4$ ,  $\text{NiO}$ ,  $\text{MnO}$ , etc.). [9,10] Following this, Li salt could be easily separated from Co, Ni, and Mn by water leaching. Researchers have experimented with many different reductants to improve Li leaching efficiency, including graphite or carbon, [11–13] glucose, [14] biomass waste, [15,16] Al, [17,18]  $\text{NH}_3$ , [19,20]  $\text{H}_2$ , [21,22] etc. Meanwhile, scientists also examine sulfation, chlorination, and nitration roasting-leaching techniques for recycling spent cathodes. [23–29] Similarly, in high-temperature reactions with sulfation agents ( $\text{H}_2\text{SO}_4$ ,  $(\text{NH}_4)_2\text{SO}_4$ ,  $\text{NiSO}_4$ ) [30–32], chlorination agents ( $\text{NH}_4\text{Cl}$ ) [26] or nitration agents ( $\text{HNO}_3$ ), [29] Li is extracted to form water-soluble  $\text{Li}_2\text{SO}_4$ ,  $\text{LiCl}$  or  $\text{LiNO}_3$ , respectively, while Co, Ni and Mn are transformed into water-insoluble oxides. Consequently, these preferentially Li-leaching strategies are able to achieve a high Li recovery ( $> 90\%$ ). However, the process of these roasting strategies still remains highly energy-consuming ( $> 500^\circ\text{C}$ ), and impurities ( $\text{Na}^+$ ,  $\text{Cl}^-$  and  $\text{SO}_4^{2-}$ ) introduced into the system would increase the costs of post-treatment. Therefore, developing an environmentally-friendly, energy-efficient and cost-effective recycling method still remains a significant challenge for sustainable battery development.

In the realm of electrocatalysis, transition-metal-based catalysts, specifically earth-abundant  $\text{Co}_3\text{O}_4$ , have been extensively studied as alternatives to commercial  $\text{RuO}_2$  or  $\text{IrO}_2$  for electrochemical oxygen evolution reaction (OER). However, the direct utilization of  $\text{Co}_3\text{O}_4$  has been hindered by its slow reaction kinetics and inadequate electronic conductivity. [33] Among the various approaches, defect engineering is a viable method to enhance the inherent OER activity through the modulation of electronic structure. [34–36] To achieve this, various techniques, such as plasma etching, [37,38] laser irradiation, [39] solvothermal/hydrothermal reduction, [40] and element doping, [41] have been successfully employed to introduce defects in  $\text{Co}_3\text{O}_4$ . The incorporation of defects, including oxygen vacancies ( $\text{V}_\text{O}$ ) and cobalt vacancies ( $\text{V}_\text{Co}$ ), into  $\text{Co}_3\text{O}_4$  can lead to the creation of unsaturated coordination sites, distortion and charge redistribution in the crystal structure. [42] Consequently, the regulated electronic configurations have the potential to effectively enhance the activity of active sites, optimize the binding energy between active sites and intermediate species, and ultimately improve the electrocatalytic performance. [43].

Building upon the aforementioned inspiration, this study sought to investigate a facile and economical approach for recycling spent LIBs and regenerating defect-enriched  $\text{Co}_3\text{O}_4$  as a highly efficient OER electrocatalyst. A low-temperature solid-to-solid reaction combined with water leaching (SSRWL) process has been utilized to successfully reclaim Li and Co from spent  $\text{LiCoO}_2$  (LCO) batteries. In a typical solid-to-solid reaction, the spent LCO was mixed with oxalic acid dihydrate powders, and underwent reduction reaction ( $> 80^\circ\text{C}$ ) that converted LCO into water-soluble lithium salts and water-insoluble cobalt salts. Through water leaching, Li was selectively extracted into water, leaving  $\text{Co}_2\text{O}_4$  as a solid residue. The remaining solid was heated to generate  $\text{Co}_3\text{O}_4$ , and diverse  $\text{Co}_3\text{O}_4$  catalysts with varying defects were obtained by cooling in different substances (furnace, air, water, liquid nitrogen). As a result, water-quenched  $\text{Co}_3\text{O}_4$  possessed the most significant defect concentration demonstrated a noteworthy performance in OER. It achieved an overpotential of 306 mV at the current density of  $10\text{ mA cm}^{-2}$  and a Tafel slop of  $55.3\text{ mV dec}^{-1}$ , even outperforming commercial  $\text{RuO}_2$  catalyst. Moreover, density functional theory (DFT) calculations verified that the presence of both  $\text{V}_\text{O}$  and  $\text{V}_\text{Co}$  could significantly decrease the energy barrier for reaction intermediates, ultimately resulting in a highly efficient OER performance.

## 2. Experimental section

### 2.1. Materials and pretreatment

The spent LCO batteries were purchased from a local energy company (Hengchuang Co., Ltd, Shenzhen). First, the batteries were discharged completely by submerging them in a 5 wt% NaCl solution. Second, the batteries were manually dismantled in a fuming hood, with the cathode, anode, separator and metal shells being separated. The spent LCO materials were then scraped off the cathode, thoroughly rinsed with deionized (DI) water and ethanol, and subsequently dried in an oven.

### 2.2. Separation of Li and Co

In a typical low-temperature solid-to-solid synthesis process, the spent LCO powders were mixed with oxalic acid dihydrate ( $\text{H}_2\text{C}_2\text{O}_4 \cdot 2\text{H}_2\text{O}$ , AR,  $\geq 99.5\%$ ) in a molar ratio of 1:5. The mixture (total weight:  $\sim 5.0\text{ g}$ ) was enclosed in a 50 mL Teflon-lined autoclave and heated at  $150^\circ\text{C}$  for 2 h. After the reaction, the autoclave underwent a natural cooling process to room temperature. The obtained product was in a paste consistency and then vacuum-dried at  $80^\circ\text{C}$  for 6 h. Following that, a water-leaching procedure was carried out by subjecting the powders to sonication in DI water for  $\sim 15\text{ min}$  with a solid-liquid ratio of  $40\text{ g L}^{-1}$ . The lithium was readily extracted into the solution, whereas the cobalt was precipitated as cobalt oxalate ( $\text{CoC}_2\text{O}_4$ ). The resulting undissolved  $\text{CoC}_2\text{O}_4$  powder was collected by suction filtration and finally dried at  $80^\circ\text{C}$  in an oven. The concentrations of Li and Co in both the leaching solution and residual solid product were analyzed using an inductively coupled plasma optical emission spectroscopy (ICP-OES, Thermo Fisher, ICAP-7200). The leaching efficiency of elements (Li, Co) was determined using the following equation:  $L = (C \times V) / (C \times V + m \times w\%)$ , where  $L$  represents the leaching efficiency (%),  $C$  is the concentration of Li and Co in the solution ( $\text{g L}^{-1}$ ),  $V$  is the volume of leaching solution,  $m$  is the weight of the solid powder after leaching, and  $w\%$  is the metal content of Li and Co in the solid powder. To enhance the effectiveness of Li leaching, the impact of various factors, including reaction temperature ( $80\text{--}200^\circ\text{C}$ ), reaction time ( $0.5\text{--}24\text{ h}$ ) and the molar ratio of  $\text{LCO}:\text{H}_2\text{C}_2\text{O}_4$  (1:1, 1:2, 1:5, 1:10, 1:15, 1:20), were investigated in the solid-solid reaction process.

### 2.3. Preparation of FC- $\text{Co}_3\text{O}_4$ -400, NC- $\text{Co}_3\text{O}_4$ -400, WQ- $\text{Co}_3\text{O}_4$ -400, and LNQ- $\text{Co}_3\text{O}_4$ -400 catalysts

To produce  $\text{Co}_3\text{O}_4$ , the as-prepared  $\text{CoC}_2\text{O}_4$  was subjected to annealing in a muffle furnace at  $400^\circ\text{C}$  for 2 h with a heating rate of  $10^\circ\text{C min}^{-1}$ . After the reaction, different cooling rates were employed, namely furnace cooling (FC), normalizing cooling (NC, air cooling), water quenching (WQ), and liquid nitrogen quenching (LNQ), with the aims of optimizing the particle size and defect concentration of  $\text{Co}_3\text{O}_4$ . As a result, four distinct samples were obtained, namely FC- $\text{Co}_3\text{O}_4$ -400, NC- $\text{Co}_3\text{O}_4$ -400, WQ- $\text{Co}_3\text{O}_4$ -400, and LNQ- $\text{Co}_3\text{O}_4$ -400.

### 2.4. Material characterization

The phase and crystal structure of the samples were characterized by a powder X-ray diffractometer (XRD, Rigaku) with  $\text{Cu-K}\alpha$  radiation ( $\lambda = 1.5405\text{ \AA}$ ). Rietveld refinements of XRD patterns were carried out by using the GSAS-II program. The concentrations of Li and Co were analyzed by ICP-OES. The morphology of the samples was examined by a field-emission scanning electron microscope (FEI PREO S(A5–112)). High-resolution transmission electron microscopy (HRTEM, JEM-200) was applied to observe the microstructure and crystal fringes of the samples. The chemical state of the samples was analyzed by an X-ray photoelectron spectroscopy (XPS, VG ESCALAB 220i-XL) with all the peaks calibrated with the  $\text{C1s}$  peak at  $284.8\text{ eV}$ .  $\text{N}_2$  adsorption/

desorption isotherms were recorded on an Autosorb-iQ Surface Area Analyzer at 77 K. Raman spectra were collected on a Renishaw 2000 Raman system. The oxygen vacancies of the as-prepared catalysts were proceeded by electron paramagnetic resonance (EPR, Bruker -EMXPlus-10) spectrometer.

## 2.5. Electrochemical measurements

The electrochemical activities of the various  $\text{Co}_3\text{O}_4$  catalysts were performed on a Metrohm Autolab electrochemical workstation with a three-electrode system at room temperature. The electrocatalytic ink was prepared by dispersing 5 mg catalyst in a mixed solvent of 1 mL isopropanol/water (4/1 v/v) and 100  $\mu\text{L}$  5 wt% Nafion solution under sonication for 30 min. The catalytic ink gradually dripped on the surface of carbon paper (CP) with a loading of approximately  $1.5 \text{ mg cm}^{-2}$  was served as the working electrode. A saturated Ag/AgCl and carbon rod were used as reference electrode and counter electrode, respectively. All the electrochemical tests were performed in 1.0 M KOH (pH=13.8). Linear sweep voltammetry (LSV) was recorded from 0.8 to 0 V (vs. Ag/AgCl) at a scan rate of  $5 \text{ mV s}^{-1}$  with iR-correction. The electrochemical surface area (ECSA) was determined by CV measurements with different scan rates ( $10\text{--}100 \text{ mV s}^{-1}$ ). Electrochemical impedance spectroscopy (EIS) measurements were carried out from 100 kHz to 0.1 Hz at the desired overpotential ( $\eta$ ) of 300 mV. Chronoamperometry measurement at fixed overpotential ( $\eta = 300 \text{ mV}$ ) was performed to evaluate the stability of the catalyst. All potentials were referenced to a reversible hydrogen electrode (RHE) according to the equation:  $E(\text{vs. RHE}) = E(\text{vs. Ag/AgCl}) + 0.197 + 0.059 \times \text{pH}$  (pH = 13.8).

## 2.6. Theoretical calculations

The density functional theory (DFT) calculations were performed on the Vienna ab initio simulation package (VASP).[44,45] The

projector-augmented wave (PAW) potentials were used to describe the interaction between core electrons and ions.[46,47] The generalized gradient approximation with the Perdew-Burke-Ernzerhof (GGA-PBE) was adopted to calculate the electron exchange-correlation.[48] Valence electrons were described by a plane wave basis set with a kinetic energy cutoff of 450 eV. Gaussian smearing method was applied for electron smearing with a width of 0.05 eV. For the structural relaxations, the energy was converged to  $1.0 \times 10^{-6} \text{ eV}$  and the force to  $0.05 \text{ eV/\AA}$ . Grimme's DFT-D3 methodology was considered for dispersion correction in all energy-related calculations.[47] A vacuum layer of 18  $\text{\AA}$  was set along the *c* direction normal to the surface plane to eliminate the periodic interactions. The Brillouin zone was sampled with a  $2 \times 2 \times 1$  Monkhorst-Pack *k*-point mesh. The  $\text{Co}_3\text{O}_4$  (311) plane was constructed as the model for surface reaction pathways. The free energy profiles were calculated on the Co sites in the optimized structure. Free energy change ( $\Delta G$ ) was estimated based on the equation[49, 50]:  $\Delta G = \Delta E + \Delta \text{ZPE} - T\Delta S$ , where *E*, ZPE, *T* and *S* are the total energy from DFT calculation, the zero-point energy, the temperature (298.15 K), and the entropy obtained from the vibrational frequency of adsorbed intermediates, respectively.

## 3. Results and discussions

### 3.1. Low-temperature solid-to-solid reaction and water-leaching process for spent LCO recycling

As illustrated in Fig. 1a, the process of extracting Li form spent LCO involves a SSRWL strategy, while defect-enriched  $\text{Co}_3\text{O}_4$  catalysts are fabricated by regulating the cooling rate during the heat treatment process. First, the spent LCO was mixed with oxalic acid dihydrate ( $\text{H}_2\text{C}_2\text{O}_4 \cdot 2\text{H}_2\text{O}$ ) powder and subsequently heated in a Teflon-lined autoclave at  $150^\circ\text{C}$ . The release of hydration water from  $\text{H}_2\text{C}_2\text{O}_4 \cdot 2\text{H}_2\text{O}$  facilitated the moistening of the powder mixture, thereby

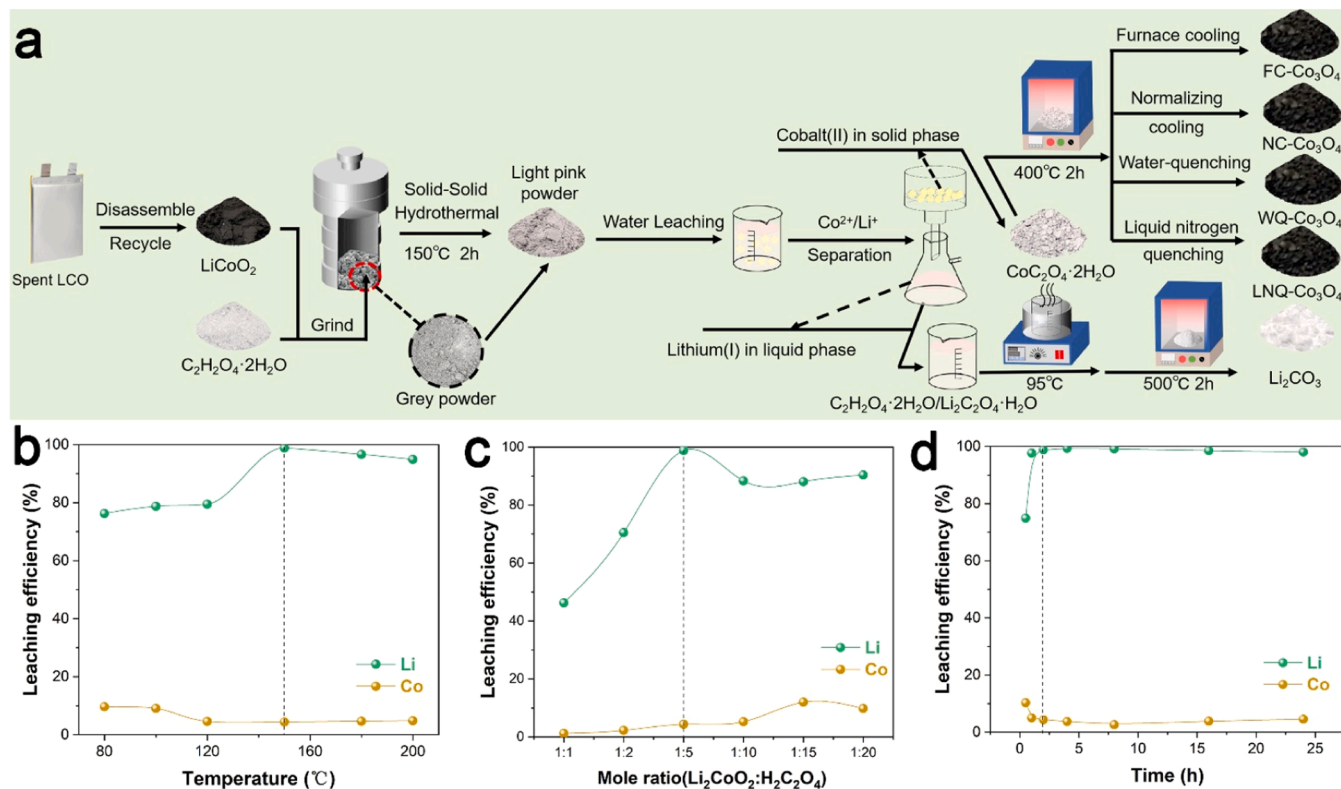
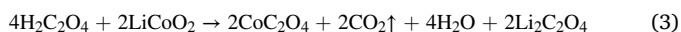
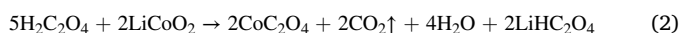


**Fig. 1.** a) Schematic procedures for a low-temperature solid-to-solid reaction combined water leaching strategy for recycling spent LCO. The effect of b) temperature (60–200  $^\circ\text{C}$ ), c)  $\text{H}_2\text{C}_2\text{O}_4 \cdot 2\text{H}_2\text{O}$  dosage and d) reaction time (0.5–24 h) on the water leaching efficiency of Li and Co.

initiating a reduction reaction between  $\text{H}_2\text{C}_2\text{O}_4$  and  $\text{LiCoO}_2$ . Additionally, the high steam pressure in the sealed space further facilitates the reduction reaction. The low-temperature solid-to-solid reaction follows the Eqs. (1–3):



After the reaction, Li and Co were readily separated using a water leaching process, with Li being extracted into the water and Co remaining in the solid residue. Thermal annealing was conducted as the final step for the preparation of  $\text{Co}_3\text{O}_4$  catalysts. Fig. S1 provides a comprehensive overview of the intermediate products and final  $\text{Co}_3\text{O}_4$  through the SSRWL strategy.

To enhance the effectiveness of Li leaching, several parameters were thoroughly investigated in the solid-to-solid reaction, including reaction temperature, molar ratio of  $\text{LCO}:\text{H}_2\text{C}_2\text{O}_4$  and reaction time. The impact of reaction temperature (60–200 °C) on the efficiency of water leaching is illustrated in Fig. 1b. A relatively low Li recovery rate ranging from 76.3% to 79.5% is observed for samples with temperature below 120 °C. This can be attributed to the incomplete reduction in Eqs. 2 or 3, as evidenced by the XRD results in Fig. S2. The efficiency of Li leaching is enhanced to 99.0% when the reaction temperature is raised to 150 °C, and subsequently remains stable at 96.0% within the temperature of 180–200 °C.  $\text{H}_2\text{C}_2\text{O}_4 \cdot 2\text{H}_2\text{O}$  dosage is another significant factor that influences the solid-to-solid reduction reaction. As depicted in Fig. 1c, the Li leaching rates of 46.2% and 70.5% are observed for  $\text{LCO}:\text{H}_2\text{C}_2\text{O}_4$  molar ratios of 1:1 and 1:2, respectively, suggesting incomplete reactions at these conditions (Fig. S3). When the  $\text{LCO}:\text{H}_2\text{C}_2\text{O}_4$  molar ratio was decreased to 1:5, the Li leaching rate achieves its maximum value of

99.0%. However, as the molar ratio of  $\text{LCO}:\text{H}_2\text{C}_2\text{O}_4$  is progressively reduced (1:10, 1:15, and 1:20), the Li leaching rate decreases to approximately 88.0%. This decrease can be ascribed to the occurrence of a side reaction between cobalt oxalate and oxalic acid.[51] The relationship between reaction time and Li leaching rate is shown in Fig. 1d. The Li leaching rate reaches 74.8% within 30 mins, rapidly increases to 97.7% in 1 h, and then stabilizes at approximately 99.0% after 2 h. This suggests that the reduction reaction is fully accomplished within 2 h at 150 °C (Fig. S4). It should be noted that a minor quantity of Co is also found in the leaching solution as a result of the slight solubility of  $\text{CoC}_2\text{O}_4$  in the acid environment.[52].

Based on the above analysis, the optimal conditions for implementing the low-temperature SSRWL strategy are as follows:  $\text{LCO}:\text{H}_2\text{C}_2\text{O}_4$  molar ratio of 1:5, reaction temperature of 150 °C and reaction time of 2 h. Consequently, under the optimum conditions, 99.0% of Li was successfully extracted into water, while 96% of Co was precipitated as solid  $\text{CoC}_2\text{O}_4 \cdot 2\text{H}_2\text{O}$ . Prior to the crystallization of Li-salts, flocculent substances were noticed in the Li-contained solution after several days of storage (Fig. S5a). This occurrence could be attributed to the reaction between impurity  $\text{Co}^{2+}$  and  $\text{C}_2\text{O}_4^{2-}$ . Following the suction filtration, a clear Li-contained solution would undergo an evaporation-crystallization process, resulting in the formation of  $\text{H}_2\text{C}_2\text{O}_4 \cdot 2\text{H}_2\text{O}$  and  $\text{LiHC}_2\text{O}_4 \cdot 2\text{H}_2\text{O}$  (Fig. S5b). The  $\text{Li}_2\text{CO}_3$  product was ultimately acquired through thermal treatment at 500 °C for 2 h in air, and the purity and crystallinity of the reclaimed product were confirmed by the XRD result (Fig. S5c). When compared to other roasting-water leaching methods (Table 1), the SSRWL strategy demonstrates its superiority in separating Li and Co from spent LCO. Moreover, the SSRWL technique offers other several benefits, such as the capability of low-temperature operation, no emission of hazardous gases and straightforward post-treatment procedures. In comparison to conventional hydrometallurgical methods, the SSRWL strategy also decreased water consumption and

**Table 1**  
Comparison of different technologies for preferentially recycling of lithium from spent LIBs.

Type of spent LIBs <sup>1</sup>	Process	Reductant or additive	Energy-consuming <sup>2</sup>	Emission of hazardous gases?	Li leaching efficiency	Water-consuming <sup>3</sup>	Ref.
LCO	<b>Solid-to-solid reaction &amp; water-leaching</b>	$\text{H}_2\text{C}_2\text{O}_4$	150 °C, low	No	99%	Medium	<b>Our work</b>
LNCMO	Reduction-roasting & water-leaching	Spent Graphite	700 °C, high	Yes	87.15%	High	[11]
LCO	Reduction-roasting & water-leaching	Glucose	550 °C, medium	Yes	97%	Medium	[14]
LNAO	Reduction-roasting & water-leaching	$\text{H}_2$	750 °C, high	Yes	94.3%	Medium	[21]
LNCMO	Reduction-roasting & water-leaching	Organics	600 °C, high	Yes	81.26%	Medium	[62]
LCO	Sulfation-roasting & water-leaching	$\text{K}_2\text{S}_2\text{O}_7$	700 °C, high	Yes	98.51%	Medium	[24]
LNCMO	Sulfation-roasting & water-leaching	$\text{Na}_2\text{SO}_4$	750 °C, high	Yes	> 85%	Medium	[63]
LCO	Nitration-roasting & water-leaching	$\text{NH}_3$	600 °C, high	Yes	> 97%	Medium	[19]
LNCMO	Reduction-roasting & water-leaching	Lignite	650 °C, high	Yes	84.7%	Medium	[64]
LCO	Chlorination-roasting & water-leaching	$\text{NH}_4\text{Cl}$	350 °C, medium	Yes	97.97%	Medium	[26]
LCO	Nitration-roasting & water-leaching	$(\text{NH}_4)_2\text{C}_2\text{O}_4$	650 °C, high	Yes	99.6%	Medium	[65]
LNCMO	Sulfation-roasting & water-leaching	$\text{NiSO}_4$	550 °C, medium	Yes	96.42%	Medium	[30]
LCO	Sulfation-roasting & water-leaching	$\text{Na}_2\text{SO}_4$	600 °C, high	Yes	92%	Medium	[66]
LNCMO	Reduction-roasting & water-leaching	$\text{H}_2$	500 °C, medium	Yes	98%	Medium	[67]
LNCMO	Reduction-roasting & water-leaching	Lignite	550 °C, medium	Yes	81%	Medium	[3]
LCO	Reduction-roasting & water-leaching	Biomass wastes	600 °C, high	Yes	99.81%	Medium	[15]
LCO	Reduction-roasting & water-leaching	Al	600 °C, high	No	93.67%	Medium	[18]
LNCMO	Sulfation-roasting & water-leaching	$(\text{NH}_4)_2\text{SO}_4$	350 °C, medium	Yes	98.5%	Medium	[31]

Note: 1. LCO:  $\text{LiCoO}_2$ , LNCMO:  $\text{LiNi}_x\text{Co}_y\text{Mn}_{(1-x-y)}\text{O}_2$ , LNAO:  $\text{LiNi}_x\text{Co}_y\text{Al}_{(1-x-y)}\text{O}_2$ .

2. Energy-consuming: high (temperature  $\geq 600$  °C), medium (temperature:200–600 °C), low (temperature < 200 °C).

3. The water consumption includes both the water used during the reaction and the post-treatment procedure.



simplified post-treatment protocols (Table S1). To obtain  $\text{Li}_2\text{CO}_3$  as the final product, a saturated  $\text{Na}_2\text{CO}_3$  is usually added to the Li-rich solution, wherein the aforementioned water-leaching and hydrometallurgical techniques are utilized. However, the overall recovery efficiency of Li is decreased by the partial dissolution of  $\text{Li}_2\text{CO}_3$  in water. This disadvantage is effectively circumvented by the SSRWL technique, in which  $\text{Li}_2\text{CO}_3$  is obtained via evaporation-crystallization and calcination procedures.

As aforementioned discussion, a sustainable and affordable recycling process is generally defined by its minimal water and energy consumable, as well as its ability to eliminate the emission of hazardous gases into the environment. Beyond this, the economic evaluation is conducted with the aim of demonstrating the financial benefits associated with the SSRWL technique. In the context of economic analysis, the primary expenses to consider are the costs of chemical reagents, electricity and water consumption, while the revenue generated comes from the production of  $\text{Li}_2\text{CO}_3$  and  $\text{Co}_3\text{O}_4$ . As depicted in Fig. S6, the entire process is divided into three distinct parts: solid-to-solid reaction (I), water leaching (II), and the formation of  $\text{Li}_2\text{CO}_3$  and  $\text{Co}_3\text{O}_4$  (III). Taking 1.0 kg of spent LCO cathode as a consideration, the final revenue of SSRWL strategy in this work is estimated to be \$12.36, significantly surpassing conventional approaches (Table S2).

### 3.2. Fabrication for deficient $\text{Co}_3\text{O}_4$ catalyst

For  $\text{Co}_3\text{O}_4$  catalyst preparation, the annealing condition of  $\text{CoC}_2\text{O}_4 \cdot 2\text{H}_2\text{O}$  was carefully tuned, as high temperatures coarsened the microstructure while low temperatures resulted in incomplete phase transformation.[53] Temperature-dependent experiment (250–500 °C) was carried out and XRD results demonstrated the complete conversion of  $\text{CoC}_2\text{O}_4$  to  $\text{Co}_3\text{O}_4$  over 300 °C in air for 2 h (Fig. S7). To achieve a balance between the morphology and crystallinity of  $\text{Co}_3\text{O}_4$ , a moderate temperature of 400 °C was applied to prepare the catalyst. The presence of vacancies in  $\text{Co}_3\text{O}_4$  could be realized by manipulating the cooling rate during the annealing process. As a result, four different defect-contained  $\text{Co}_3\text{O}_4$  by cooling the samples in the furnace, air, water and liquid nitrogen were obtained, namely, FC- $\text{Co}_3\text{O}_4$ -400, NC- $\text{Co}_3\text{O}_4$ -400, WQ- $\text{Co}_3\text{O}_4$ -400 and LNQ- $\text{Co}_3\text{O}_4$ -400. Fig. S8 shows the surface morphologies of the reclaimed  $\text{CoC}_2\text{O}_4$  and defect-enriched  $\text{Co}_3\text{O}_4$ .  $\text{CoC}_2\text{O}_4$  exhibited well-crystallized nanoplate structure (Fig. S8a-b), while FC- $\text{Co}_3\text{O}_4$ -400, NC- $\text{Co}_3\text{O}_4$ -400, WQ- $\text{Co}_3\text{O}_4$ -400 and LNQ- $\text{Co}_3\text{O}_4$ -400 all display tiny nanoparticle structures (Fig. S8c-j).

Detailed morphology characterization is further investigated by TEM observation, as shown in Fig. 2. Four different  $\text{Co}_3\text{O}_4$  catalysts exhibit a comparable mesoporous structure comprising of tiny subunits but with

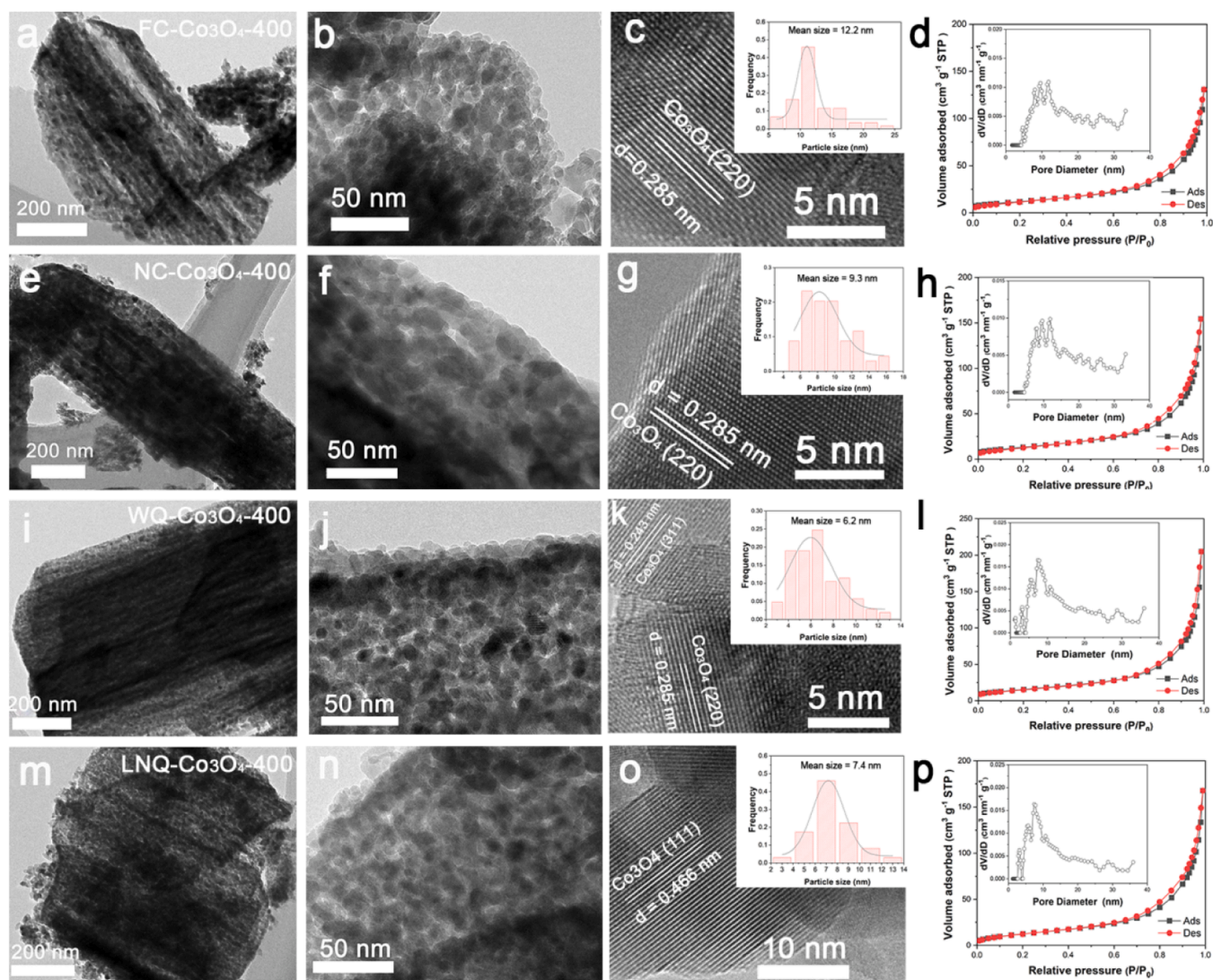


**Fig. 2.** TEM and HRTEM images of a-c) FC- $\text{Co}_3\text{O}_4$ -400, e-g) NC- $\text{Co}_3\text{O}_4$ -400, i-k) WQ- $\text{Co}_3\text{O}_4$ -400 and m-o) LNQ- $\text{Co}_3\text{O}_4$ -400. The inset is the corresponding statistic particle size distribution of subunits.  $\text{N}_2$  adsorption-desorption isotherms of d) FC- $\text{Co}_3\text{O}_4$ -400, h) NC- $\text{Co}_3\text{O}_4$ -400, j) WQ- $\text{Co}_3\text{O}_4$ -400 and p) LNQ- $\text{Co}_3\text{O}_4$ -400. The inset corresponds to the pore size distribution curves.

varying particle dimensions. The mean sizes of the subunit are determined to be 12.2 nm, 9.3 nm, 6.2 nm and 7.4 nm for FC-Co<sub>3</sub>O<sub>4</sub>-400, NC-Co<sub>3</sub>O<sub>4</sub>-400, WQ-Co<sub>3</sub>O<sub>4</sub>-400 and LNQ-Co<sub>3</sub>O<sub>4</sub>-400, respectively. The result reveals a significant correlation between the cooling rate and the subunit size of the catalysts. Generally, the size of the Co<sub>3</sub>O<sub>4</sub> subunits decreases as the cooling rate increases. However, it is not applied to the samples cooling in water and liquid nitrogen. The potential explanation can be ascribed to the dissolution effect of hot Co<sub>3</sub>O<sub>4</sub> during water quenching process. The confirmation of dissolution effect was achieved by the ICP observation of Co in water, which is estimated to be 0.3287 mg L<sup>-1</sup> (Table S2). The uneven dissolution of Co also results in the formation of Co defective sites within Co<sub>3</sub>O<sub>4</sub>. The lattice fringes with interplanar d-spacing of 0.285 nm and 0.466 nm are ascribed to the (220) and (111) planes of Co<sub>3</sub>O<sub>4</sub>, respectively.[54] The surface area and pore size distribution of FC-Co<sub>3</sub>O<sub>4</sub>-400, NC-Co<sub>3</sub>O<sub>4</sub>-400, WQ-Co<sub>3</sub>O<sub>4</sub>-400, and LNQ-Co<sub>3</sub>O<sub>4</sub>-400 are determined by the nitrogen adsorption-desorption isotherm, as shown in Fig. 2d, h, i and p. All the samples display a type-IV sorption isotherm with a hysteresis loop, indicating the mesoporous structure of the fabricated samples. WQ-Co<sub>3</sub>O<sub>4</sub>-400 exhibits a surface area of 56.2 m<sup>2</sup> g<sup>-1</sup>, which is much higher than that of FC-Co<sub>3</sub>O<sub>4</sub>-400 (43.0 m<sup>2</sup> g<sup>-1</sup>), NC-Co<sub>3</sub>O<sub>4</sub>-400 (46 m<sup>2</sup> g<sup>-1</sup>) and LNQ-Co<sub>3</sub>O<sub>4</sub>-400 (48.3 m<sup>2</sup> g<sup>-1</sup>). The pore size distribution is calculated based on the DFT method. Observation reveals that the fabricated samples display a predominant presence of pores within the 5–30 nm range, further confirming their mesoporous characteristics. Additionally, it is observed that both LNQ-Co<sub>3</sub>O<sub>4</sub>-400 and WQ-Co<sub>3</sub>O<sub>4</sub>-400 contain a small number of pores less than 2 nm. This suggests that the rapid cooling process also contributes to the formation of micropores within the sample. The hierarchical porous structures not only offer sufficient active sites for OER but also provide a quick pathway for reactant transportation.

The crystal structures of FC-Co<sub>3</sub>O<sub>4</sub>-400, NC-Co<sub>3</sub>O<sub>4</sub>-400, WQ-Co<sub>3</sub>O<sub>4</sub>-400, and LNQ-Co<sub>3</sub>O<sub>4</sub>-400 catalysts were characterized by X-ray diffraction (XRD) analysis. The peaks at 19.0, 31.2, 36.8, 38.5, 44.8, 55.7, 59.3 and 65.2° are observed for (111), (220), (311), (222), (400),

(331), (422), (511) and (440) planes, respectively, which can be ascribed to the cubic spinel Co<sub>3</sub>O<sub>4</sub> (PDF #43-1003, space group: *Fd*  $\bar{3}$  *m*). A negligible and weak peak around 26–27° was occasionally observed, possibly due to the presence of carbon residues in the cathode materials. Rietveld refinement of the XRD patterns is further employed to analyze and compare the structure parameters of different Co<sub>3</sub>O<sub>4</sub> catalysts, as illustrated in Fig. S9 and Table S3. The presence of oxygen vacancies (V<sub>O</sub>) can be ascertained by examining the occupancy rates of O sites, whereas the occurrence of cobalt vacancies (V<sub>Co</sub>) are dependent on Co1 (Co<sup>2+</sup>, tetrahedral sites) and Co2 (Co<sup>3+</sup>, octahedral sites) occupancies.[55] The WQ-Co<sub>3</sub>O<sub>4</sub>-400 has a lower percentage of occupied O sites (99.0%) compared to FC-Co<sub>3</sub>O<sub>4</sub>-400 (99.9%), NC-Co<sub>3</sub>O<sub>4</sub>-400 (99.6%), and LNQ-Co<sub>3</sub>O<sub>4</sub>-400 (99.2%), suggesting a higher concentration of V<sub>O</sub>. The findings indicate that the V<sub>O</sub> content is significantly influenced by the cooling rate and cooling medium. Furthermore, the occupancy rates of Co below 1.0 indicate the presence of V<sub>Co</sub> in WQ-Co<sub>3</sub>O<sub>4</sub>-400. Accordingly, the chemical formulas are refined to be Co<sub>3</sub>O<sub>3.996</sub>, Co<sub>3</sub>O<sub>3.984</sub>, Co<sub>2.995</sub>O<sub>3.960</sub> and Co<sub>3</sub>O<sub>3.969</sub> for FC-Co<sub>3</sub>O<sub>4</sub>-400, NC-Co<sub>3</sub>O<sub>4</sub>-400, WQ-Co<sub>3</sub>O<sub>4</sub>-400, and LNQ-Co<sub>3</sub>O<sub>4</sub>-400, respectively. Moreover, with increasing the V<sub>O</sub> content, the charge valence state in Co<sub>3</sub>O<sub>4</sub> can be altered by reducing the smaller ionic radius Co<sup>3+</sup> (0.55 Å) to larger Co<sup>2+</sup> (0.61 Å),[55] as confirmed by the Co<sup>3+</sup>/Co<sup>2+</sup> ratio and lattice parameters (Table S4). The decreased Co<sup>3+</sup>/Co<sup>2+</sup> ratio also suggests that the V<sub>O</sub> sites are predominantly incorporated in the vicinity of the Co<sup>3+</sup> sites.

The electronic structure and chemical states of FC-Co<sub>3</sub>O<sub>4</sub>-400, NC-Co<sub>3</sub>O<sub>4</sub>-400, WQ-Co<sub>3</sub>O<sub>4</sub>-400, and LNQ-Co<sub>3</sub>O<sub>4</sub>-400 were characterized by X-ray photoelectron spectroscopy (XPS). The C, Co and O elements are identified in the survey spectra of all the samples (Fig. 3b). In the O 1s high-resolution XPS spectra (Fig. 3c), all the samples exhibit three different peaks at 530.0, 531.4 and 532.8 eV, which can be contributed to lattice oxygen (O<sub>L</sub>), vacancy oxygen (O<sub>V</sub>) and OH-adsorbed oxygen (O<sub>H</sub>), respectively.[56] The proportion of O<sub>L</sub>, O<sub>V</sub> and O<sub>H</sub> is determined by the area enclosed by their peaks in the deconvoluted O 1s peaks. As shown in Table S5, the O<sub>V</sub> occupies 21.8%, 24.9%, 30.3% and 26.5% for

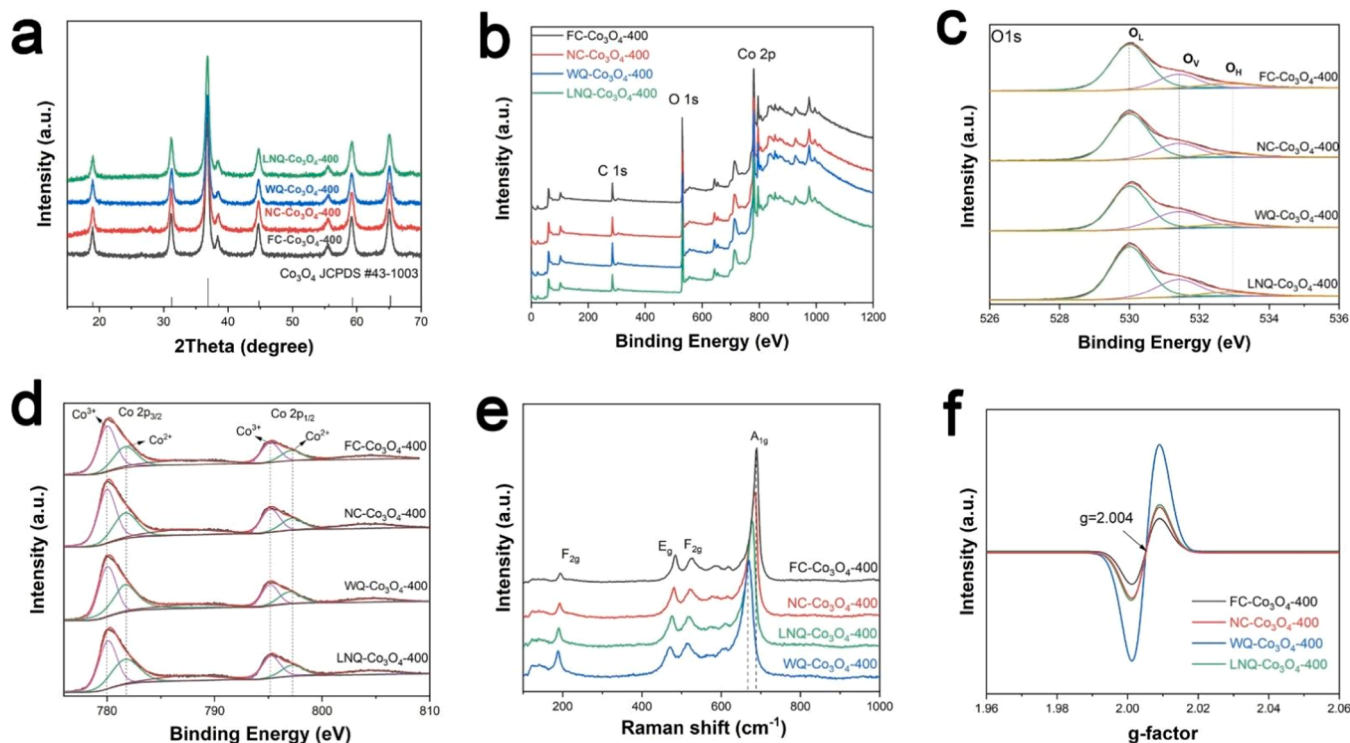
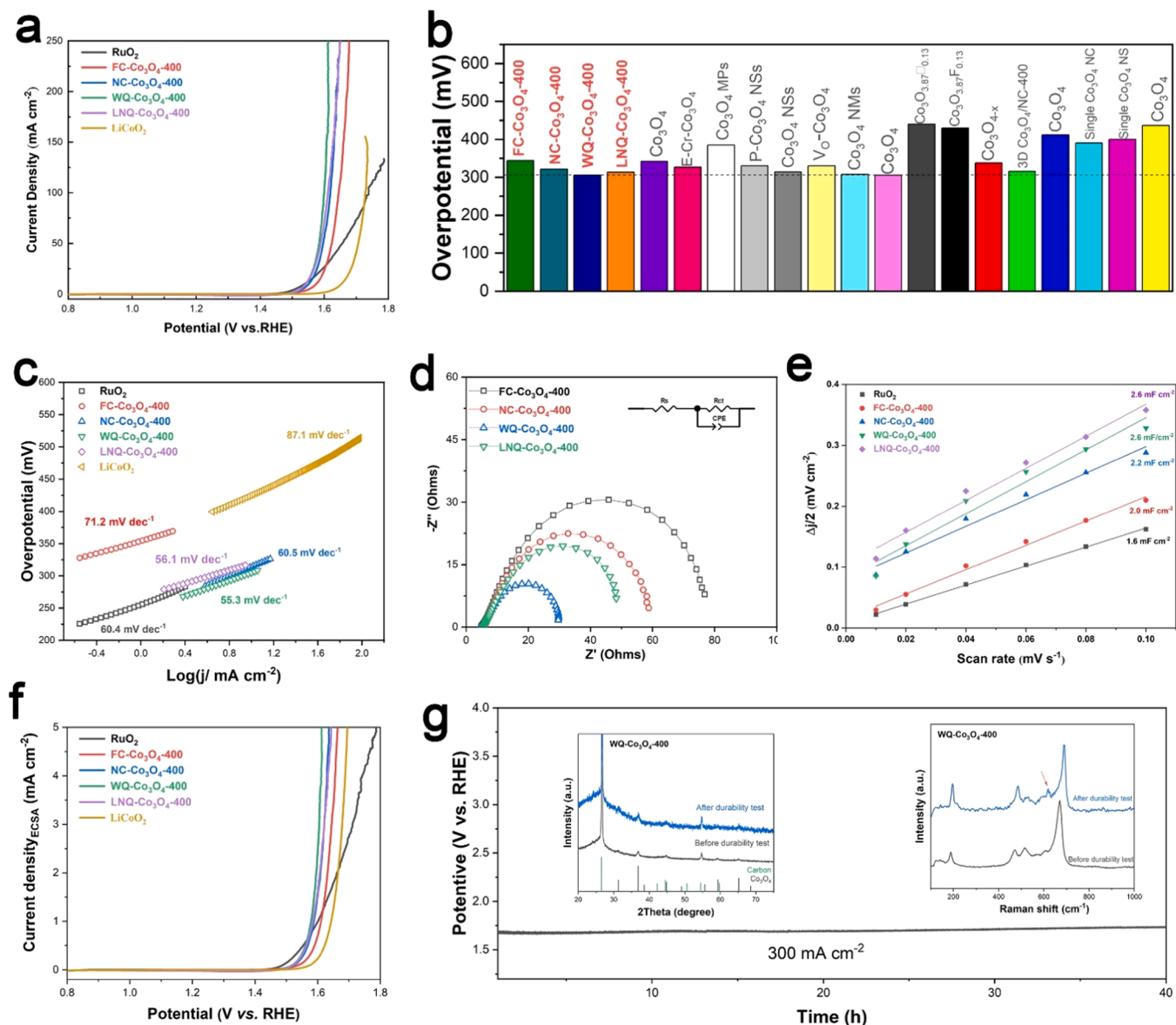


Fig. 3. a) XRD patterns, b) survey XPS spectra, high-resolution XPS spectra of c) O 1s and d) Co 2p, e) Raman spectra and f) EPR spectra of FC-Co<sub>3</sub>O<sub>4</sub>-400, NC-Co<sub>3</sub>O<sub>4</sub>-400, WQ-Co<sub>3</sub>O<sub>4</sub>-400 and LNQ-Co<sub>3</sub>O<sub>4</sub>-400.

FC-Co<sub>3</sub>O<sub>4</sub>-400, NC-Co<sub>3</sub>O<sub>4</sub>-400, WQ-Co<sub>3</sub>O<sub>4</sub>-400, and LNQ-Co<sub>3</sub>O<sub>4</sub>-400, respectively. In general, the content of O<sub>V</sub> increases with the cooling rate. This can be explained by the limited duration for the healing of defects within the crystals at high cooling rates. The higher O<sub>V</sub> content in WQ-Co<sub>3</sub>O<sub>4</sub>-400 than in LNQ-Co<sub>3</sub>O<sub>4</sub>-400 can be ascribed to the water dissolution as aforementioned. The XPS analysis demonstrates a congruent outcome with the refined XRD. Fig. 3d shows the deconvolution of the Co 2p XPS spectra. The peaks at 779.9 and 795.3 eV represent the Co 2p<sub>3/2</sub> and 2p<sub>1/2</sub> of Co<sup>3+</sup> in Co<sub>3</sub>O<sub>4</sub>, [54] while the other two peaks at 781.7 and 797.3 eV are attributed to Co 2p<sub>3/2</sub> and 2p<sub>1/2</sub> of Co<sup>2+</sup> in Co<sub>3</sub>O<sub>4</sub>. [55,57] The broad peaks at 786.4 and 804.6 eV are ascribed to the Co 2p<sub>3/2</sub> and 2p<sub>1/2</sub> satellite peaks, respectively. [58] Additionally, the Co<sup>3+</sup>/Co<sup>2+</sup> ratio by the XPS fitting results are 1.72, 1.63, 1.02 and 1.44 for FC-Co<sub>3</sub>O<sub>4</sub>-400, NC-Co<sub>3</sub>O<sub>4</sub>-400, WQ-Co<sub>3</sub>O<sub>4</sub>-400, and LNQ-Co<sub>3</sub>O<sub>4</sub>-400 (Table S5), respectively. The results indicate that the presence of O<sub>V</sub> can change the valence state of Co in Co<sub>3</sub>O<sub>4</sub> by

decreasing the Co<sup>3+</sup>/Co<sup>2+</sup> ratio, and WQ-Co<sub>3</sub>O<sub>4</sub>-400 has an even lower Co<sup>3+</sup>/Co<sup>2+</sup> ratio, potentially because of the Co<sup>3+</sup> ions dissolved in water during the fabrication process. This agrees well with the Rietveld XRD analysis.

Fig. 3e shows the Raman spectra of FC-Co<sub>3</sub>O<sub>4</sub>-400, NC-Co<sub>3</sub>O<sub>4</sub>-400, WQ-Co<sub>3</sub>O<sub>4</sub>-400, and LNQ-Co<sub>3</sub>O<sub>4</sub>-400. The peaks at 194.1, 483.7, 525.5, and 689.4 cm<sup>-1</sup> are ascribed to F<sub>2g</sub>, E<sub>g</sub>, F<sub>2g</sub> and A<sub>1g</sub> modes of Co<sub>3</sub>O<sub>4</sub>, respectively. [33,59,60] In addition, a peak shift is observed for Co<sub>3</sub>O<sub>4</sub> samples with different V<sub>O</sub> and V<sub>Co</sub>. In the case of A<sub>1g</sub> modes, the wave number reduces from 689.4 cm<sup>-1</sup> in FC-Co<sub>3</sub>O<sub>4</sub>-400 to 684.1 cm<sup>-1</sup> in NC-Co<sub>3</sub>O<sub>4</sub>-400, 670.2 cm<sup>-1</sup> in WQ-Co<sub>3</sub>O<sub>4</sub>-400, and 678.6 cm<sup>-1</sup> in LNQ-Co<sub>3</sub>O<sub>4</sub>-400, respectively. The observed shift towards lower wave numbers can be attributed to the distortion of the lattice structure and the presence of oxygen vacancies. [34,42,57] Besides, the O<sub>V</sub> content of different samples can be determined by the EPR analysis (Fig. 3f). The observed g-factor of 2.004 is ascribed to the oxygen vacancies with



**Fig. 4.** Electrocatalytic OER activity of the prepared catalysts. a) iR-corrected polarization curves of FC-Co<sub>3</sub>O<sub>4</sub>-400, NC-Co<sub>3</sub>O<sub>4</sub>-400, WQ-Co<sub>3</sub>O<sub>4</sub>-400, LNQ-Co<sub>3</sub>O<sub>4</sub>-400, commercial RuO<sub>2</sub> and pristine LCO in 1.0 M KOH electrolyte at a scan rate of 5 mV/s. b) Comparison of  $\eta_{10}$  for our catalysts and other Co<sub>3</sub>O<sub>4</sub> catalysts. c) Tafel plots of the catalysts obtained from their corresponding polarization curve results. d) Nyquist plots of the catalysts at an overpotential of 300 mV for OER. e) Current densities versus scan rates measured at a potential value of 0.95 V (vs. RHE) for different catalysts. f) Polarization curves of the samples with current density normalized to the ECSA. g) Chronopotentiometric measurements of WQ-Co<sub>3</sub>O<sub>4</sub>-400 catalyst for OER process at a current density of 300 mA cm<sup>-2</sup> for 40 h with Hg/HgO as the reference electrode. The insets in g are the corresponding XRD and Raman patterns of WQ-Co<sub>3</sub>O<sub>4</sub>-400 catalyst on carbon paper after durability test.



unpaired electrons.[36] It is noteworthy that the intensity of the WQ-Co<sub>3</sub>O<sub>4</sub>-400 is significantly stronger compared to those of FC-Co<sub>3</sub>O<sub>4</sub>-400, NC-Co<sub>3</sub>O<sub>4</sub>-400 and LNQ-Co<sub>3</sub>O<sub>4</sub>-400, thereby indicating its higher O<sub>V</sub> content in WQ-Co<sub>3</sub>O<sub>4</sub>-400.

### 3.3. Electrochemical properties of defective Co<sub>3</sub>O<sub>4</sub>

The electrocatalytic activities of the catalysts towards OER are evaluated in an alkaline electrolyte (1.0 M KOH) in a typical three-electrode system. All the measured potentials in this work are calibrated to the reversible hydrogen electrode (RHE). According to the polarization curves (Fig. 4a), WQ-Co<sub>3</sub>O<sub>4</sub>-400 exhibits a lower overpotential at 10 mA cm<sup>-2</sup> ( $\eta_{10}$  = 306 mV) than FC-Co<sub>3</sub>O<sub>4</sub>-400, NC-Co<sub>3</sub>O<sub>4</sub>-400, LNQ-Co<sub>3</sub>O<sub>4</sub>-400 and pristine LCO (344, 321, 313 and 423 mV, respectively). Notably, the low  $\eta_{10}$  of WQ-Co<sub>3</sub>O<sub>4</sub>-400 even outperforms that of benchmark RuO<sub>2</sub> ( $\eta_{10}$  = 309 mV). Likewise, WQ-Co<sub>3</sub>O<sub>4</sub>-400 also exhibits excellent OER activities at high current densities ( $\eta_{20}$  = 326 mV,  $\eta_{50}$  = 352 mV and  $\eta_{100}$  = 369 mV), much lower than those of NC-Co<sub>3</sub>O<sub>4</sub>-400, LNQ-Co<sub>3</sub>O<sub>4</sub>-400, pristine LCO and FC-Co<sub>3</sub>O<sub>4</sub>-(250, 300, 350, 400, 450 and 500) (Figs. S10-11). When compared to other Co<sub>3</sub>O<sub>4</sub>-based catalysts, WQ-Co<sub>3</sub>O<sub>4</sub>-400 obtained in this work still exhibits exceptional OER performance (Fig. 4b and Table S6-S7). In addition, the outstanding OER activity of WQ-Co<sub>3</sub>O<sub>4</sub>-400 is also reflected by the lowest Tafel slope of 55.3 mV dec<sup>-1</sup> in comparison to those of FC-Co<sub>3</sub>O<sub>4</sub>-400 (71.2 mV dec<sup>-1</sup>), NC-Co<sub>3</sub>O<sub>4</sub>-400 (60.5 mV dec<sup>-1</sup>), LNQ-Co<sub>3</sub>O<sub>4</sub>-400 (56.1 mV dec<sup>-1</sup>), RuO<sub>2</sub> (60.4 mV dec<sup>-1</sup>), pristine LCO (87.1 mV dec<sup>-1</sup>) (Fig. 4c) and other FC-Co<sub>3</sub>O<sub>4</sub> catalysts (Fig. S11c). The low Tafel slope suggests a high reaction kinetics for OER process. The precise reaction kinetics across the active materials was further evaluated by the electrochemical impedance spectra (EIS) measurement (Fig. 4d). According to the established equivalent circuit and fitted Nyquist plots, WQ-Co<sub>3</sub>O<sub>4</sub>-400 displays the smallest charge transfer resistance ( $R_{ct}$ ) of 28.7  $\Omega$  compared to those of FC-Co<sub>3</sub>O<sub>4</sub>-400 (83.6  $\Omega$ ), NC-Co<sub>3</sub>O<sub>4</sub>-400 (58.3  $\Omega$ ) and LNQ-Co<sub>3</sub>O<sub>4</sub>-400 (36.4  $\Omega$ ), suggesting that it possesses the fastest charge transfer rate for OER reaction.

To better clarify the OER performance of the prepared catalysts, the electrochemical active surface area (ECSA) was estimated based on the double-layer capacitance ( $C_{dl}$ ) determined by CV curves at various scan rates (0.01–0.2 V s<sup>-1</sup>) (Fig. S12). As shown in Fig. 4e, WQ-Co<sub>3</sub>O<sub>4</sub>-400 and LNQ-Co<sub>3</sub>O<sub>4</sub>-400 exhibit a larger  $C_{dl}$  value (2.6 mF cm<sup>-2</sup>) than those of FC-Co<sub>3</sub>O<sub>4</sub>-400 (2.0 mF cm<sup>-2</sup>), NC-Co<sub>3</sub>O<sub>4</sub>-400 (2.2 mF cm<sup>-2</sup>), RuO<sub>2</sub> (1.6 mF cm<sup>-2</sup>), pristine LCO (0.43 mF cm<sup>-2</sup>) and other FC-Co<sub>3</sub>O<sub>4</sub> catalysts (Fig. S13-14). To better evaluate and compare the intrinsic activity of different catalysts, the OER current densities are normalized by the calculated ECSA (Fig. 4f). At a designated overpotential of 350 mV, WQ-Co<sub>3</sub>O<sub>4</sub>-400 shows the highest specific activity (1.24 mA cm<sup>-2</sup><sub>ECSA</sub>), which is nearly 3.4, 1.6 and 1.4 times higher than those of FC-Co<sub>3</sub>O<sub>4</sub>-400 (0.36 mA cm<sup>-2</sup><sub>ECSA</sub>), NC-Co<sub>3</sub>O<sub>4</sub>-400 (0.76 mA cm<sup>-2</sup><sub>ECSA</sub>) and LNQ-Co<sub>3</sub>O<sub>4</sub>-400 (0.89 mA cm<sup>-2</sup><sub>ECSA</sub>), respectively (Fig. S15). Moreover, WQ-Co<sub>3</sub>O<sub>4</sub>-400 also delivers a higher intrinsic activity than commercial RuO<sub>2</sub> catalyst (0.77 mA cm<sup>-2</sup><sub>ECSA</sub>), pristine LCO (0.11 mA cm<sup>-2</sup><sub>ECSA</sub>) and other FC-Co<sub>3</sub>O<sub>4</sub> catalysts (Fig. S15-17). BET-normalized current densities were also calculated to evaluate the activities of different catalysts (Fig. S18), in which WQ-Co<sub>3</sub>O<sub>4</sub>-400 also outperformed that of FC-Co<sub>3</sub>O<sub>4</sub>-400, NC-Co<sub>3</sub>O<sub>4</sub>-400 and LNQ-Co<sub>3</sub>O<sub>4</sub>-400.

The aforementioned findings demonstrate the coexistence of V<sub>O</sub> and V<sub>Co</sub> can effectively boost the catalytic activity of spined Co<sub>3</sub>O<sub>4</sub>. In addition to the OER performance, the reclaimed Co<sub>3</sub>O<sub>4</sub> from the spent LCO also exhibits its price advantage in practical applications. The durability is another crucial criterion to evaluate the OER performance of catalysts during the practical application. The long-term stability was evaluated by chronopotentiometry with a current density of 300 mA cm<sup>-2</sup> for 40 h. As plotted in Fig. 4g, no obvious undulation of potential is observed after long-time testing, indicating the high stability of WQ-Co<sub>3</sub>O<sub>4</sub>-400. Furthermore, the notable stability of the catalysts was also evidenced by the absence of any discernible phase change after

the durability test (inset XRD patterns in Fig. 4g). A slightly peak shift was detected in the Raman spectrum (inset Raman patterns in Fig. 4g), which could be attributed to the surface structure evolution after the durability test.[42] A new emerged peak at ~ 615 cm<sup>-1</sup> indicates the chemical bonding of abundant hydroxide groups on the surface after long-term durability test.[42] The durability of WQ-Co<sub>3</sub>O<sub>4</sub>-400 was also demonstrated by chronoamperometry (Fig. S19) and polarization curves before and after 1000 cycles (Fig. S20).

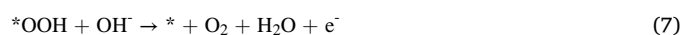
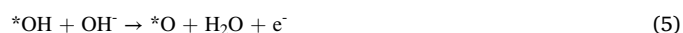
### 3.4. DFT calculations

To further understand the underlying effect of V<sub>O</sub> and V<sub>Co</sub> towards OER in the Co<sub>3</sub>O<sub>4</sub> catalyst, a theoretical study was employed based on DFT calculations. Based on prior studies, it has been suggested that the V<sub>O</sub> site may become saturated with \*OH, which subsequently transforms into lattice OH under OER potential.[42] As a result, the V<sub>O</sub> site may present challenges in facilitating a four-electron OER process. On the surface of defect-free Co<sub>3</sub>O<sub>4</sub>, the Co<sup>3+</sup> site exhibits greater affinity for \*OH and \*OOH adsorption compared to the Co<sup>2+</sup> site. Additionally, the Co<sup>3+</sup> site displays a reduced overpotential of 0.5 eV in contrast to the 0.76 eV observed at the Co<sup>2+</sup> site, based on the Gibbs free energy diagram for the OER process (Fig. S21a-b). This lower overpotential suggests a greater propensity for the OER process to occur at the Co<sup>3+</sup> site. Through the integration of XPS and refined XRD analysis, it is evident that the V<sub>O</sub> sites are predominantly incorporated in the vicinity of the Co<sup>3+</sup> sites. Consequently, the creation of vacancies and DFT calculation of four-electron OER process were all centered on the Co<sup>3+</sup> site.

The creation of V<sub>O</sub> and V<sub>Co</sub> is achieved through removing O or Co atoms from a spinel Co<sub>3</sub>O<sub>4</sub> structure, and the vacancy concentration is determined by the number of removed atoms. To simplify the subsequent calculation, modifications are made to a Co<sub>3</sub>O<sub>4</sub> supercell (60 Co atoms and 80 O atoms) by removing one, two and three O atoms to represent FC-Co<sub>3</sub>O<sub>4</sub>-400, NC-Co<sub>3</sub>O<sub>4</sub>-400 and LNQ-Co<sub>3</sub>O<sub>4</sub>-400, respectively. Additionally, WQ-Co<sub>3</sub>O<sub>4</sub>-400 is modelled by removing four O atoms and one Co atoms. The optimized models for FC-Co<sub>3</sub>O<sub>4</sub>-400, NC-Co<sub>3</sub>O<sub>4</sub>-400, WQ-Co<sub>3</sub>O<sub>4</sub>-400 and LNQ-Co<sub>3</sub>O<sub>4</sub>-400 are shown in Fig. 5a. The formation of V<sub>O</sub> or V<sub>Co</sub> in FC-Co<sub>3</sub>O<sub>4</sub>-400, NC-Co<sub>3</sub>O<sub>4</sub>-400, WQ-Co<sub>3</sub>O<sub>4</sub>-400 and LNQ-Co<sub>3</sub>O<sub>4</sub>-400 is an endothermic process with a formation energy of 1.07 eV, 0.73 eV, 0.54 eV and 0.63 eV, respectively (Fig. S22). The lower formation energy indicates a more stable structure.

The H<sub>2</sub>O adsorption energy for Co<sup>3+</sup> reactive site was calculated and compared across various local chemical environment, as illustrated in Fig. S21c. Evidently, the Co<sup>3+</sup> site, upon removal of four O atoms and one Co atoms, exhibits a more pronounced negative water adsorption energy of -0.73 eV compared to other samples. The result indicates WQ-Co<sub>3</sub>O<sub>4</sub>-400 ensure effective water adsorption and subsequent four-electron OER process. Furthermore, examination of project of density of states (pDOS) and band center of the surface atom indicates an elevation of Co 3d band center from -1.82 eV for defect-free Co<sub>3</sub>O<sub>4</sub> to -1.32 eV for WQ-Co<sub>3</sub>O<sub>4</sub>-400 (Fig. S21d). This leads to a decrease in electron filling of the antibonding orbitals and is expected to result in stronger chemical bonds between the Co<sup>3+</sup> site and adsorbed oxygen-containing intermediates.

A typical four-electron reaction pathway was used to clarify the basic principles of the OER process. Under alkaline conditions, the reaction steps are as follows (Eqs. 4-7)[61]:



where \* is the active site of the catalysts, \*OH, \*O and \*OOH are the reaction intermediates. The detailed processes of the adsorbed reaction



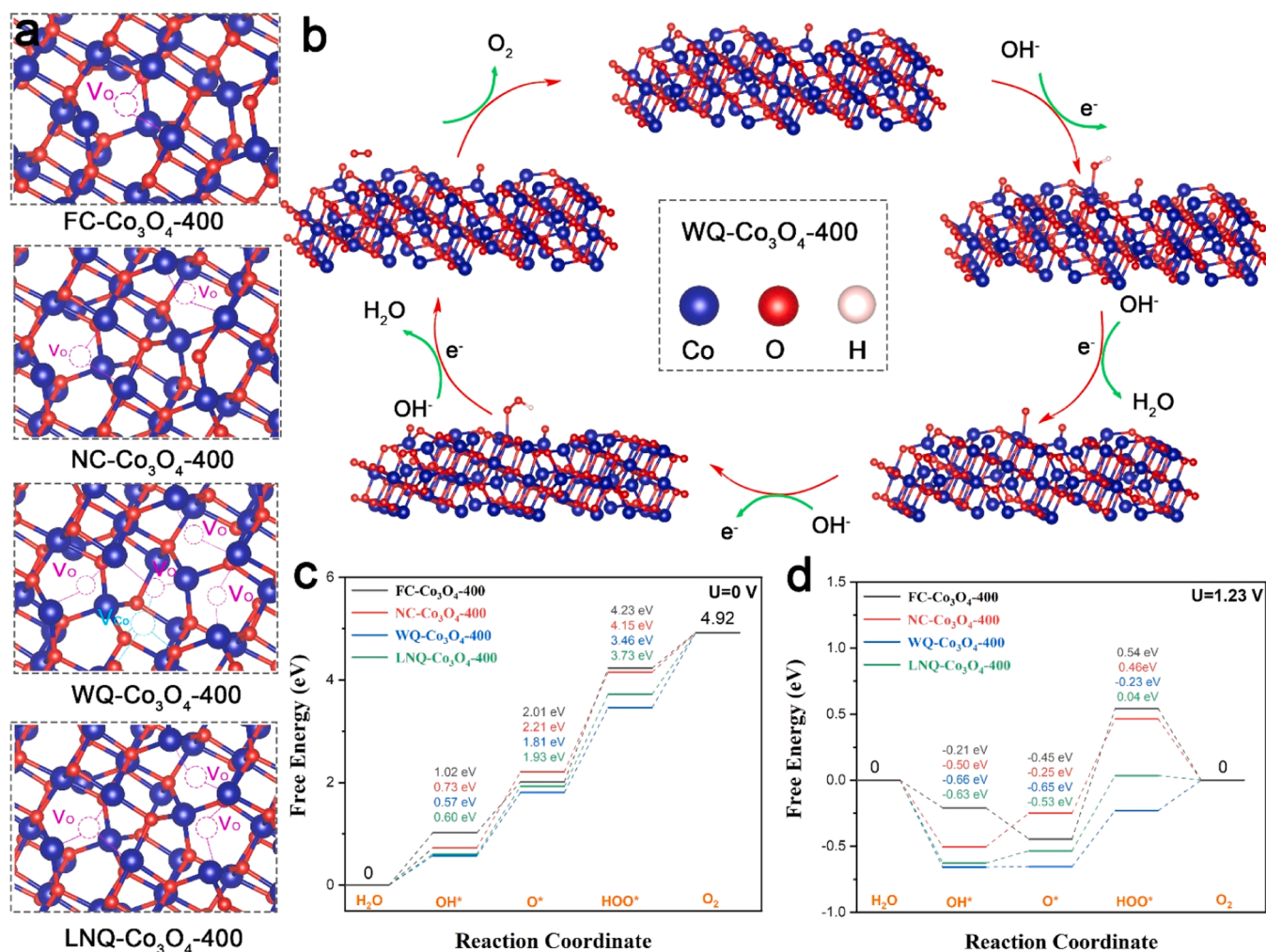


**Fig. 5.** a) Optimized structures of (311) surface for FC-Co<sub>3</sub>O<sub>4</sub>-400, NC-Co<sub>3</sub>O<sub>4</sub>-400, WQ-Co<sub>3</sub>O<sub>4</sub>-400 and LNQ-Co<sub>3</sub>O<sub>4</sub>-400. b) Schematic illustration of optimized active intermediates adsorption structures for a typical four-electron reaction on the surface of WQ-Co<sub>3</sub>O<sub>4</sub>-400 slab. The Gibbs free energy diagram of the OER process for FC-Co<sub>3</sub>O<sub>4</sub>-400, NC-Co<sub>3</sub>O<sub>4</sub>-400, WQ-Co<sub>3</sub>O<sub>4</sub>-400 and LNQ-Co<sub>3</sub>O<sub>4</sub>-400 at c) zero potential ( $U = 0$  V) and d) equilibrium potential ( $U = 1.23$  V).

intermediates on the surface of the defected Co<sub>3</sub>O<sub>4</sub> are schematically illustrated in Fig. 5b. The absorption Gibbs free energy of each step is calculated to provide a comprehensive understanding of the reaction mechanism of the different catalysts, as shown in Fig. 5c-d. All the steps exhibit uphill absorption energy, suggesting endothermic reactions when the bias potential is zero ( $U = 0$  V). Specifically, FC-Co<sub>3</sub>O<sub>4</sub>-400 shows the highest Gibbs free energy of \*OH (1.02 eV) and \*OOH (4.23 eV) intermediates, indicating the sluggish reaction for the OER process. The coexistence of V<sub>O</sub> and V<sub>Co</sub> can greatly facilitate OH adsorption and promote the corresponding OER process, providing low free energies of 0.57 eV and 3.46 eV for \*OH and \*OOH intermediates, respectively. The potential determining steps (PDS) for the Co sites are calculated and all the defected Co<sub>3</sub>O<sub>4</sub> catalysts show the same limiting steps as in the transformation from \*O to \*OOH. The PDS Gibbs free energy change ( $\Delta G_{\text{PDS}}$ ) for FC-Co<sub>3</sub>O<sub>4</sub>-400 is 2.22 eV and decreases to 1.94 eV (NC-Co<sub>3</sub>O<sub>4</sub>-400) and 1.80 eV (LNQ-Co<sub>3</sub>O<sub>4</sub>-400) with increasing V<sub>O</sub> content in Co<sub>3</sub>O<sub>4</sub>. For WQ-Co<sub>3</sub>O<sub>4</sub>-400, it shows the lowest  $\Delta G_{\text{PDS}}$  of 1.65 eV, suggesting the lowest energy barrier and best OER performance with the coexistence of V<sub>O</sub> and V<sub>Co</sub>. Furthermore, when the applied potential is increased to 1.23 V ( $U = 1.23$  V, the equilibrium potential), the formation of \*OH and \*O shows Gibbs free energy downhill. The PDS is still the formation of \*OOH, and the  $\Delta G_{\text{PDS}}$  for FC-Co<sub>3</sub>O<sub>4</sub>-400, NC-Co<sub>3</sub>O<sub>4</sub>-400, WQ-Co<sub>3</sub>O<sub>4</sub>-400 and LNQ-Co<sub>3</sub>O<sub>4</sub>-400 are 0.99 eV, 0.71 eV, 0.42 eV and 0.57 eV, respectively. Therefore, the DFT calculations reveal a remarkable improvement in the OER performance of spinel

Co<sub>3</sub>O<sub>4</sub> by inducing V<sub>O</sub> and V<sub>Co</sub>, showing consistent results with our experimental testing.

#### 4. Conclusion

In conclusion, a facile low-temperature SSRWL strategy has been successfully achieved for effectively recycling spent LiCoO<sub>2</sub> batteries. On the basis of the reduction reaction, the spent LiCoO<sub>2</sub> materials are completely converted into water-soluble Li salts and water-insoluble Co<sub>2</sub>O<sub>4</sub> at 150 °C for 2 h. After water leaching, 99% Li is extracted into the solution and 96% Co remained in the solid. Li<sub>2</sub>CO<sub>3</sub> is recovered without significant lost via evaporation-crystallization and calcination procedures. Besides the high recovery rates, the straightforward post-treatment steps and low water and energy consumption make the SSRWL approach highly capable for practical applications. Defective Co<sub>3</sub>O<sub>4</sub> catalysts are prepared by cooling the samples in furnace, air, water and liquid nitrogen. The V<sub>O</sub> concentration is directly related to the cooling rate, while the V<sub>Co</sub> is successfully incorporated by water quenching procedure. Physicochemical characterization demonstrates that the water quenched catalyst (WQ-Co<sub>3</sub>O<sub>4</sub>-400) possesses the highest surface area and defect concentration among the different catalysts. Consequently, OER measurement in alkaline solution reveals that WQ-Co<sub>3</sub>O<sub>4</sub>-400 delivers superior electrochemical performance, even outperforming the benchmark RuO<sub>2</sub>. The systematically experimental and theoretical results unveil the coexistence of V<sub>O</sub> and V<sub>Co</sub> accelerates the

reaction kinetics and lower the reaction barrier for the intermediates formation. This study presents a promising, cost-effective and energy-efficient strategy for recycling spent LIBs. Additionally, is demonstrates a straightforward technique for constructing defective structures in high-performance catalysts for electrochemical water splitting.

### CRediT authorship contribution statement

**Feng Cao:** Investigation, Data curation. **Jie Pan:** Investigation, Data curation. **Jie Liu:** Writing – review & editing, Validation, Supervision, Resources, Project administration, Funding acquisition, Formal analysis. **Binbin Zhou:** Resources, Investigation, Formal analysis. **Zheming Zhang:** Writing – review & editing, Supervision, Resources, Project administration, Funding acquisition. **Jianbin Lin:** Investigation, Data curation. **Haidong Bian:** Writing – review & editing, Writing – original draft, Validation, Supervision, Resources, Project administration, Methodology, Funding acquisition, Formal analysis, Conceptualization. **Jing Zhong:** Validation, Software, Investigation, Formal analysis, Data curation. **Zebiao Li:** Validation, Resources, Investigation, Funding acquisition, Formal analysis, Data curation. **Zhizhou Wang:** Visualization, Validation, Software, Investigation, Formal analysis, Data curation.

### Declaration of Competing Interest

The authors declare that they have no known competing financial interests or personal relationships that could have appeared to influence the work reported in this paper.

### Data availability

Data will be made available on request.

### Acknowledgements

We acknowledge the financial support from the National Natural Science Foundation of China (21702143, 52303092), and Guangdong Basic and Applied Basic Research Foundation Special Projects-Guangdong-Shenzhen Joint Funds (2022A1515110027). Thanks eceshi ([www.eceshi.com](http://www.eceshi.com)) for the XPS, EPR, TEM tests and theoretical calculations. The authors would also like to thank Shiyanjia Lab ([www.shiyanjia.com](http://www.shiyanjia.com)) for XRD refinement.

### Appendix A. Supporting information

Supplementary data associated with this article can be found in the online version at [doi:10.1016/j.apcatb.2024.123873](https://doi.org/10.1016/j.apcatb.2024.123873).

### References

- [1] Battery 2030: Resilient, sustainable, and circular. <https://www.mckinsey.com/industries/automotive-and-assembly/our-insights/battery-2030-resilient-sustainable-and-circular>.
- [2] X. Zhu, J. Xiao, Q. Mao, Z. Zhang, Z. You, L. Tang, Q. Zhong, A promising regeneration of waste carbon residue from spent Lithium-ion batteries via low-temperature fluorination roasting and water leaching, *Chem. Eng. J.* 430 (2022) 132703.
- [3] J. Zhang, G. Liang, C. Yang, J. Hu, Y. Chen, C. Wang, A breakthrough method for the recycling of spent lithium-ion batteries without pre-sorting, *Green. Chem.* 23 (2021) 8434–8440.
- [4] Z.J. Baum, R.E. Bird, X. Yu, J. Ma, Lithium-ion battery recycling—overview of techniques and trends, *ACS Energy Lett.* 7 (2022) 712–719.
- [5] H. Lv, H. Huang, C. Huang, Q. Gao, Z. Yang, W. Zhang, Electric field driven delithiation: A strategy towards comprehensive and efficient recycling of electrode materials from spent lithium ion batteries, *Appl. Catal., B* 283 (2021) 119634.
- [6] C. Huang, H. Lv, Z. Yang, C. Lian, J. Du, G. Liu, W. Tang, Z. Xu, Z. Chi, H. Liu, H. Huang, W. Zhang, Exfoliating spent cathode materials with robust interlayer interactions into atomic-thin nanosheets for boosting the oxygen evolution reaction, *J. Mater. Chem. A* 10 (2022) 3359–3372.
- [7] T. Georgi-Maschler, B. Friedrich, R. Weyhe, H. Heegn, M. Rutz, Development of a recycling process for Li-ion batteries, *J. Power Sources* 207 (2012) 173–182.
- [8] C.M. Costa, J.C. Barbosa, R. Gonçalves, H. Castro, F.J.D. Campo, S. Lanceros-Méndez, Recycling and environmental issues of lithium-ion batteries: advances, challenges and opportunities, *Energy Stor. Mater.* 37 (2021) 433–465.
- [9] B. Makuza, Q. Tian, X. Guo, K. Chattopadhyay, D. Yu, Pyrometallurgical options for recycling spent lithium-ion batteries: a comprehensive review, *J. Power Sources* 491 (2021) 229622.
- [10] M. Zhou, B. Li, J. Li, Z. Xu, Pyrometallurgical technology in the recycling of a spent lithium ion battery: evolution and the challenge, *ACS EST Eng.* 1 (2021) 1369–1382.
- [11] G. Zhang, X. Yuan, C.Y. Tay, Y. He, H. Wang, C. Duan, Selective recycling of lithium from spent lithium-ion batteries by carbothermal reduction combined with multistage leaching, *Sep. Purif. Technol.* 314 (2023) 123555.
- [12] K. Huang, H. Xiong, H. Dong, Y. Liu, Y. Lu, K. Liu, J. Wang, Carbon thermal reduction of waste ternary cathode materials and wet magnetic separation based on Ni/MnO nanocomposite particles, *Process Saf. Environ. Prot.* 165 (2022) 278–285.
- [13] T. Rostami, B. Khoshandam, S. Maroufi, Recovery of lithium, cobalt, nickel, and manganese from spent lithium-ion batteries through a wet-thermal process, *Mater. Res. Bull.* 153 (2022) 111897.
- [14] B. Zhang, Y. Xu, B. Makuza, F. Zhu, H. Wang, N. Hong, Z. Long, W. Deng, G. Zou, H. Hou, X. Ji, Selective lithium extraction and regeneration of LiCoO<sub>2</sub> cathode materials from the spent lithium-ion battery, *Chem. Eng. J.* 452 (2023) 139258.
- [15] X. Chen, Y. Wang, S. Li, Y. Jiang, Y. Cao, X. Ma, Selective recycling of valuable metals from waste LiCoO<sub>2</sub> cathode material of spent lithium-ion batteries through low-temperature thermochemistry, *Chem. Eng. J.* 434 (2022) 134542.
- [16] X. Liu, Y. Ma, X. Zhou, J. Yang, H. Kang, Y. He, J. Tang, F. Su, W. Yang, Y. Zhang, Reduction mechanism of bamboo powder pyrolysis in selective lithium extraction from spent lithium-ion batteries, *J. Environ. Chem. Eng.* 11 (2023) 110172.
- [17] W. Wang, Y. Zhang, L. Zhang, S. Xu, Cleaner recycling of cathode material by in-situ thermite reduction, *J. Clean. Prod.* 249 (2020) 119340.
- [18] W. Wang, Y. Zhang, X. Liu, S. Xu, A simplified process for recovery of Li and Co from spent LiCoO<sub>2</sub> cathode using Al foil as the in situ reductant, *ACS Sustain. Chem. Eng.* 7 (2019) 12222–12230.
- [19] J. Xiao, B. Niu, Z. Xu, Ammonia reduction system for the diversity of cathode processing of Li-ion batteries, *ACS Sustain. Chem. Eng.* 9 (2021) 12091–12099.
- [20] Y. Ma, J. Tang, R. Wanaldi, X. Zhou, H. Wang, C. Zhou, J. Yang, A promising selective recovery process of valuable metals from spent lithium ion batteries via reduction roasting and ammonia leaching, *J. Hazard. Mater.* 402 (2021) 123491.
- [21] J.S. Park, S. Seo, K. Han, S. Lee, M.J. Kim, A process using a thermal reduction for producing the battery grade lithium hydroxide from wasted black powder generated by cathode active materials manufacturing, *J. Hazard. Mater.* 448 (2023) 130952.
- [22] H. Pinegar, R. Marthi, P. Yang, Y.R. Smith, Reductive thermal treatment of LiCoO<sub>2</sub> from end-of-life lithium-ion batteries with hydrogen, *ACS Sustain. Chem. Eng.* 9 (2021) 7447–7453.
- [23] C. Yang, J. Zhang, Z. Cao, Q. Jing, Y. Chen, C. Wang, Sustainable and facile process for lithium recovery from spent LiNi<sub>1-x</sub>Co<sub>x</sub>Mn<sub>2</sub>O<sub>2</sub> cathode materials via selective sulfation with ammonium sulfate, *ACS Sustain. Chem. Eng.* 8 (2020) 15732–15739.
- [24] C. Liu, H. Ji, J. Liu, P. Liu, G. Zeng, X. Luo, Q. Guan, X. Mi, Y. Li, J. Zhang, Y. Tong, Z. Wang, S. Wu, An emission-free controlled potassium pyrosulfate roasting-assisted leaching process for selective lithium recycling from spent Li-ion batteries, *Waste Manag. (Oxf.)* 153 (2022) 52–60.
- [25] C. Liu, J. Lin, H. Cao, Y. Zhang, Z. Sun, Recycling of spent lithium-ion batteries in view of lithium recovery: a critical review, *J. Clean. Prod.* 228 (2019) 801–813.
- [26] E. Fan, L. Li, J. Lin, J. Wu, J. Yang, F. Wu, R. Chen, Low-temperature molten-salt-assisted recovery of valuable metals from spent lithium-ion batteries, *ACS Sustain. Chem. Eng.* 7 (2019) 16144–16150.
- [27] J. Xiao, R. Gao, B. Niu, Z. Xu, Study of reaction characteristics and controlling mechanism of chlorinating conversion of cathode materials from spent lithium-ion batteries, *J. Hazard. Mater.* 407 (2021) 124704.
- [28] Y. Jian, Z. Zongliang, Z. Gang, J. Liangxing, L. Fangyang, J. Ming, L. Yanqing, Process study of chloride roasting and water leaching for the extraction of valuable metals from spent lithium-ion batteries, *Hydrometallurgy* 203 (2021) 105638.
- [29] C. Peng, F. Liu, Z. Wang, B.P. Wilson, M. Lundström, Selective extraction of lithium (Li) and preparation of battery grade lithium carbonate (Li<sub>2</sub>CO<sub>3</sub>) from spent Li-ion batteries in nitrate system, *J. Power Sources* 415 (2019) 179–188.
- [30] J. Lin, C. Cui, X. Zhang, E. Fan, R. Chen, F. Wu, L. Li, Closed-loop selective recycling process of spent LiNi<sub>1-x</sub>Co<sub>x</sub>Mn<sub>1-x-y</sub>O<sub>2</sub> batteries by thermal-driven conversion, *J. Hazard. Mater.* 424 (2022) 127757.
- [31] Y. Tang, X. Qu, B. Zhang, Y. Zhao, H. Xie, J. Zhao, Z. Ning, P. Xing, H. Yin, Recycling of spent lithium nickel cobalt manganese oxides via a low-temperature ammonium sulfate roasting approach, *J. Clean. Prod.* 279 (2021) 123633.
- [32] Y. Tang, B. Zhang, H. Xie, X. Qu, P. Xing, H. Yin, Recovery and regeneration of lithium cobalt oxide from spent lithium-ion batteries through a low-temperature ammonium sulfate roasting approach, *J. Power Sources* 474 (2020) 228596.
- [33] L. Xia, L. Bo, W. Shi, Y. Zhang, Y. Shen, X. Ji, X. Guan, Y. Wang, J. Tong, Defect and interface engineering of templated synthesis of hollow porous Co<sub>3</sub>O<sub>4</sub>/CoMoO<sub>4</sub> with highly enhanced electrocatalytic activity for oxygen evolution reaction, *Chem. Eng. J.* 452 (2023) 139250.
- [34] J. Guo, G. Wang, S. Cui, B. Xia, Z. Liu, S.-q. Zang, Vacancy and strain engineering of Co<sub>3</sub>O<sub>4</sub> for efficient water oxidation, *J. Colloid Interface Sci.* 629 (2023) 346–354.
- [35] C.-Z. Yuan, H.-R. Zhao, S.-Y. Huang, L. Zhang, J. Li, Y. Weng, Z.-T. Sun, X. Zhang, S. Ye, Y. Chen, Promoting the activation of H<sub>2</sub>O via vacancy defects over metal-organic framework-derived cobalt oxide for enhanced oxygen evolution, *Int. J. Hydrog. Energy* (2023).

- [36] X. Yang, J. Cheng, H. Li, Y. Xu, W. Tu, J. Zhou, Self-supported N-doped hierarchical  $\text{Co}_3\text{O}_4$  electrocatalyst with abundant oxygen vacancies for acidic water oxidation, *Chem. Eng. J.* 465 (2023) 142745.
- [37] Y.-C. Huang, W. Chen, Z. Xiao, Z. Hu, Y.-R. Lu, J.-L. Chen, C.-L. Chen, H.-J. Lin, C.-T. Chen, K.T. Arul, S. Wang, C.-L. Dong, W.-C. Chou, In situ/operando soft X-ray spectroscopic identification of a  $\text{Co}^{4+}$  intermediate in the oxygen evolution reaction of defective  $\text{Co}_3\text{O}_4$  nanosheets, *J. Phys. Chem. Lett.* 13 (2022) 8386–8396.
- [38] M. Yuan, J. Jiang, F. Xue, J. Deng, Y. Dai, L. Li, M. Cui, X. Qiao, Z. Fei, Plasma-engraved  $\text{Co}_3\text{O}_4$  nanostructure toward improved formaldehyde oxidation performance: insight into the structure–activity relationship, *Appl. Surf. Sci.* 600 (2022) 154183.
- [39] H. Hu, Q. Li, L. Li, X. Teng, Z. Feng, Y. Zhang, M. Wu, J. Qiu, Laser irradiation of electrode materials for energy storage and conversion, *Matter* 3 (2020) 95–126.
- [40] Z. Cai, Y. Bi, E. Hu, W. Liu, N. Dwarica, Y. Tian, X. Li, Y. Kuang, Y. Li, X.-Q. Yang, H. Wang, X. Sun, Single-crystalline ultrathin  $\text{Co}_3\text{O}_4$  nanosheets with massive vacancy defects for enhanced electrocatalysis, *Adv. Energy Mater.* 8 (2018) 1701694.
- [41] Z. Wang, W. Xu, X. Chen, Y. Peng, Y. Song, C. Lv, H. Liu, J. Sun, D. Yuan, X. Li, X. Guo, D. Yang, L. Zhang, Defect-rich nitrogen doped  $\text{Co}_3\text{O}_4/\text{C}$  porous nanocubes enable high-efficiency bifunctional oxygen electrocatalysis, *Adv. Funct. Mater.* 29 (2019) 1902875.
- [42] R. Zhang, L. Pan, B. Guo, Z.-F. Huang, Z. Chen, L. Wang, X. Zhang, Z. Guo, W. Xu, K.P. Loh, J.-J. Zou, Tracking the role of defect types in  $\text{Co}_3\text{O}_4$  structural evolution and active motifs during oxygen evolution reaction, *J. Am. Chem. Soc.* 145 (2023) 2271–2281.
- [43] Y. Zhang, H. Liu, S. Zhao, C. Xie, Z. Huang, S. Wang, Insights into the dynamic evolution of defects in electrocatalysts, *Adv. Mater.* 35 (2023) 2209680.
- [44] G. Kresse, J. Furthmüller, Efficient iterative schemes for ab initio total-energy calculations using a plane-wave basis set, *Phys. Rev. B* 54 (1996) 11169–11186.
- [45] J.P. Perdew, K. Burke, M. Ernzerhof, Generalized gradient approximation made simple, *Phys. Rev. Lett.* 77 (1996) 3865–3868.
- [46] P.E. Blöchl, Projector augmented-wave method, *Phys. Rev. B* 50 (1994) 17953–17979.
- [47] S. Grimme, J. Antony, S. Ehrlich, H. Krieg, A consistent and accurate ab initio parametrization of density functional dispersion correction (DFT-D) for the 94 elements H–Pu, *J. Chem. Phys.* 132 (2010) 154104.
- [48] G. Kresse, D. Joubert, From ultrasoft pseudopotentials to the projector augmented-wave method, *Phys. Rev. B* 59 (1999) 1758–1775.
- [49] J. Rossmeisl, A. Logadottir, J.K. Nørskov, Electrolysis of water on (oxidized) metal surfaces, *Chem. Phys.* 319 (2005) 178–184.
- [50] J.K. Nørskov, J. Rossmeisl, A. Logadottir, L. Lindqvist, J.R. Kitchin, T. Bligaard, H. Jónsson, Origin of the overpotential for oxygen reduction at a fuel-cell cathode, *J. Phys. Chem. B* 108 (2004) 17886–17892.
- [51] L. Sun, K. Qiu, Organic oxalate as leachant and precipitant for the recovery of valuable metals from spent lithium-ion batteries, *Waste Manag. (Oxf.)* 32 (2012) 1575–1582.
- [52] X. Zeng, J. Li, B. Shen, Novel approach to recover cobalt and lithium from spent lithium-ion battery using oxalic acid, *J. Hazard. Mater.* 295 (2015) 112–118.
- [53] H. Bian, W. Wu, Y. Zhu, C.H. Tsang, Y. Cao, J. Xu, X. Liao, Z. Lu, X.-Y. Lu, C. Liu, Z. Zhang, Waste to treasure: regeneration of porous Co-based catalysts from spent  $\text{LiCoO}_2$  cathode materials for an efficient oxygen evolution reaction, *ACS Sustain. Chem. Eng.* 11 (2023) 670–678.
- [54] Q. Zhang, P. Yang, H. Zhang, J. Zhao, H. Shi, Y. Huang, H. Yang, Oxygen vacancies in  $\text{Co}_3\text{O}_4$  promote  $\text{CO}_2$  photoreduction, *Appl. Catal., B* 300 (2022) 120729.
- [55] H. Zeng, Mh Oubla, X. Zhong, N. Alonso-Vante, F. Du, Y. Xie, Y. Huang, J. Ma, Rational defect and anion chemistries in  $\text{Co}_3\text{O}_4$  for enhanced oxygen evolution reaction, *Appl. Catal., B* 281 (2021) 119535.
- [56] X. Zhang, D. Wu, X. Liu, Y. Qiu, Z. Liu, H. Xie, J. Duan, B. Hou, Efficient electrocatalytic chlorine evolution under neutral seawater conditions enabled by highly dispersed  $\text{Co}_3\text{O}_4$  catalysts on porous carbon, *Appl. Catal., B* 330 (2023) 122594.
- [57] C.-Z. Yuan, S. Wang, K. San Hui, K. Wang, J. Li, H. Gao, C. Zha, X. Zhang, D. A. Dinh, X.-L. Wu, Z. Tang, J. Wan, Z. Shao, K.N. Hui, In situ immobilizing atomically dispersed Ru on oxygen-defective  $\text{Co}_3\text{O}_4$  for efficient oxygen evolution, *ACS Catal.* 13 (2023) 2462–2471.
- [58] T. Tran-Phu, R. Daiyan, J. Leverett, Z. Fusco, A. Tadich, I. Di Bernardo, A. Kiy, T. N. Truong, Q. Zhang, H. Chen, P. Kluth, R. Amal, A. Tricoli, Understanding the activity and stability of flame-made  $\text{Co}_3\text{O}_4$  spinels: A route towards the scalable production of highly performing OER electrocatalysts, *Chem. Eng. J.* 429 (2022) 132180.
- [59] G. Li, Z. Shui, X. Duan, H. Yang, Z. Zhao, T. Zhao, Z. Zhang, G. Jiang, H. Ren, J. Cheng, Z. Hao, Unveiling the balance between catalytic activity and water resistance over  $\text{Co}_3\text{O}_4$  catalysts for propane oxidation: the role of crystal facet and oxygen vacancy, *ACS Catal.* 13 (2023) 237–247.
- [60] Z. Liu, H.M.A. Amin, Y. Peng, M. Corva, R. Pentcheva, K. Tschulik, Facet-dependent intrinsic activity of single  $\text{Co}_3\text{O}_4$  nanoparticles for oxygen evolution reaction, *Adv. Funct. Mater.* 33 (2023) 2210945.
- [61] D. Zhou, P. Li, W. Xu, S. Jawaid, J. Mohammed-Ibrahim, W. Liu, Y. Kuang, X. Sun, Recent advances in non-precious metal-based electrodes for alkaline water electrolysis, *ChemNanoMat* 6 (2020) 336–355.
- [62] G. Zhang, Z. Liu, X. Yuan, Y. He, N. Wei, H. Wang, B. Zhang, Recycling of valuable metals from spent cathode material by organic pyrolysis combined with in-situ thermal reduction, *J. Hazard. Mater.* 430 (2022) 128374.
- [63] D. Chang, S. Yang, P. Shi, Y. Jie, F. Hu, G. Fang, Y. Chen, Selective recovery of lithium and efficient leaching of transition metals from spent  $\text{LiNi}_{0.8}\text{Co}_{0.1}\text{Mn}_{0.1}\text{O}_2$  batteries based on a synergistic roasting process, *Chem. Eng. J.* 449 (2022) 137752.
- [64] J. Hu, J. Zhang, H. Li, Y. Chen, C. Wang, A promising approach for the recovery of high value-added metals from spent lithium-ion batteries, *J. Power Sources* 351 (2017) 192–199.
- [65] C. Liu, P. Liu, H. Xu, G. Zeng, X. Luo, Z. Wang, L. Yang, C. Deng, J. He, Oriented conversion of spent  $\text{LiCoO}_2$ -lithium battery cathode materials to high-value products via thermochemical reduction with common ammonium oxalate, *Resour. Conserv. Recycl.* 190 (2023) 106782.
- [66] P. Xu, C. Liu, X. Zhang, X. Zheng, W. Lv, F. Rao, P. Yao, J. Wang, Z. Sun, Synergic mechanisms on carbon and sulfur during the selective recovery of valuable metals from spent lithium-ion batteries, *ACS Sustain. Chem. Eng.* 9 (2021) 2271–2279.
- [67] F. Liu, C. Peng, Q. Ma, J. Wang, S. Zhou, Z. Chen, B.P. Wilson, M. Lundström, Selective lithium recovery and integrated preparation of high-purity lithium hydroxide products from spent lithium-ion batteries, *Sep. Purif. Technol.* 259 (2021) 118181.